Effect of Winglet Serration Geometry on the Wingtip Vortex

P. Gehlert *, K. Sabnis †, H. Babinsky ‡
University of Cambridge, Cambridge, United Kingdom, CB2 1PZ

The effect of serrations applied to the top edge of a winglet on the wingtip vortex is explored experimentally using dye-flow visualisation and stereoscopic particle image velocimetry. The wing is towed in a water tank at a chord-based Reynolds number of 100 000 and four different serration edge patterns are compared to a baseline winglet featuring a single shedding edge. The chevron winglets tested feature a triangular and sinusoidal shedding edge of the same wavelength, a multi-scale geometry imposed on the underlying triangular pattern as well as a short-wavelength triangular shedding edge, where the wavelength is reduced by half. The serrations of the wingtip are found to shed two distinct vortices from the peak and troughs of the pattern that subsequently merge around 10 chord lengths downstream of the wing. The merging process is thought to be the dominant contributor to the observed change in vortex structure. The resulting vortex features a lower swirl velocity as well as a larger vortex core compared to the vortex shed by the baseline endplate. These effects persist until at least 155 and 70 chord lengths downstream of the wingtip when the wing is at an angle of attack of 3° and 12°, respectively. Applying a sinusoidal or fractal pattern has a negligible effect on the vortex when compared to the underlying triangular wave pattern. In contrast, modifying the wavelength of the serrations has a significant effect on the vortex structure, where the short-wavelength triangular pattern displays the biggest reduction in swirl velocity and core radius increase.

I. Introduction

When bound circulation leaves a lifting wing, it rolls up into a region of vortical flow that is approximately centred around the tip of the wing and is thus referred to as a wingtip vortex. Through a phenomenon commonly referred to as induced drag, this vortex reduces the efficiency of the wing by rotating the lift vector direction away from the vertical. Moreover, the wingtip vortex significantly affects the aerodynamics of any downstream object. This may be another lifting surface, as often seen in race car aerodynamics, where multiple vortices and wings are located in close proximity [1] and where the downwash from a vortex may increase the effective angle of attack of a downstream wing such that it stalls, as well as in aircraft engines, where the tip vortex impinges on downstream blades [2]. Alternatively, a wingtip vortex may also pose significant risk to downstream aircraft, pushing them to the extremes (and beyond) of their handling capabilities. Due to an insufficient understanding about the complex nature of wingtip vortex decay, conservative estimates are necessary when deciding on aircraft landing intervals [3]. This in turn can lead to long holding patterns, which increases the environmental and financial footprint of aviation.

Understanding the development of wingtip vortices and subsequently controlling their properties therefore provides significant opportunities for optimised aerodynamics. In doing so, the central aim of any design decision is to weaken the vortex by reducing its tangential (or swirl) velocity or to completely destroy it. One way in which to alter a wingtip vortex is to subject it to turbulent flow. Here, Sarpkaya and Daly [4] associated an increased turbulence intensity of the surrounding freestream with a quicker vortex decay. In more detail, Melander and Hussain [5] showed that azimuthal strain imposed on the initially isotropic turbulent surrounding by the vortex creates 'secondary structures' that drain rotational energy from the main vortex. Similar observations were made in simulations by Holzäpfel et al. [6], who noted a weakening of the main vortex during the formation of these secondary structures. Similarly, Bailey and Tavoularis [7] measured a reduction in the maximum tangential velocity at the same core radius when the wingtip vortex was released into a flow with sufficient freestream turbulence. Once more, azimuthally aligned 'secondary structures' that strip vorticity from the main vortex, or create a transfer of angular momentum, were proposed as possible explanations.

*Research associate, pg469@cam.ac.uk, Department of Engineering, University of Cambridge
†Research associate, Department of Engineering, Cambridge of University
‡Professor of Aerodynamics, Department of Engineering, University of Cambridge, AIAA Fellow

Since controlling the ambient fluid is not always possible, a more direct approach to impacting the properties of the wingtip vortex is based on modifying the shedding edge along which the vortex forms. Initial approaches focused on attaching simple vertical flat plates to the wingtip. These winglets (or endplates) reduce the pressure gradient along the shedding edge as well as spread out the distance over which circulation of the wing is released, thereby lowering the peak rotational velocity of the vortex. Furthermore, by displacing the vortex away from the wing, its impact on the wing itself is restricted and the induced drag is reduced [8, 9]. As a result, winglets have now become the norm in civil aviation.

In a bid to further reduce the effect of the wingtip vortex by causing a more rapid dissipation, more exotic approaches have also been investigated. To name a few, wingtip sails, where a cascade of fanned small wings jut out in a radial pattern from the tip edge [10, 11] or spiroid winglets [12], aim to weaken the rotational flow by splitting the wingtip vortex into individual structures. Alternative methods to dynamically dampen the vortex have focused on local blowing and suction [13]. Yet another class of techniques to mitigate the wingtip vortex introduce turbulence into the vortex, in a bid to increase the size of the viscous core and therefore lower the peak swirl velocity. A passive element (in the form of a stalled vortex generator) which increases local turbulence at the wingtip has been observed to enlarge the vortex core by up to five times [14] and flight tests of porous wingtips showed reductions in maximum rotational velocity of up to 70 % in close proximity to the wing, although this reduced to 10 % several hundred metres further downstream [15]. A likely reason for the modifications having lower impact at these higher downstream locations is that the effects of the turbulence introduced into the viscous core do not persist over long streamwise distances, perhaps due to a relaminarization of the core [16] or perturbations within the core being suppressed by inertial waves [17].

A more novel method to reduce the impact of wingtip vortices through flow dispersion is found in the form of fractal geometries. Rather than shedding vorticity at a single lengthscale, fractal patterns distribute the energy over a range of scales [18–21]. Moreover, serrated and multi-scale trailing edge patterns on wings have equally shown a reduction in shedding energy at small enough chevron angles [22, 23]. These same serrated and multi-scale patterns, graphically illustrated in figure 1, may therefore provide an opportunity to significantly affect the wingtip vortex, through a comparably small geometric change. Rather than shedding a single coherent vortex from a straight-edged winglet, a fractal pattern applied to the top edge of an endplate releases vortices of various lengthscales. Here, a preliminary study, focusing on the effect of serrated and fractal patterns applied to an endplate, shows that the coherence of the shed vortex is dramatically affected within the measurement domain which extended to 3.5 chord lengths downstream of the wingtip [24]. Moreover, Goyal and Nedić [25] reported a reduction in vortex swirl just behind the wingtip when increasing the amplitude (and in turn the chevron angle) of serrations applied to the tip of a flat plate at incidence. The authors argue that this reduction is driven by streamwise turbulent fluctuations created by chevron pattern.

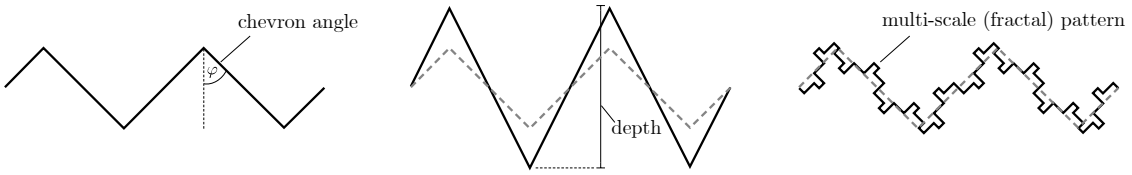

Fig. 1 Serration patterns

The previous work on chevron patterns applied to the shedding edge of a wing, relies on various core design choices that invoke a number of unanswered questions. In general, the studied chevron patterns all feature straight edges and sharp corners, yet the effect of a smoother transition has not been studied. The question therefore remains whether the sharpness of the edges plays an important roll? Secondly, data from Nedi and Vassilicos [22] and Goyal and Nedić [25] suggest that 'deeper' serrations change the structure of released vorticity. It however remains unclear whether this is due to a larger vertical spacing between shed vortical structures or whether it is instead the chevron angle itself that is the governing parameter? Thirdly, multi-scale patterns are thought to distribute energy over a larger range of scales and thereby lead to a more isotropic flow. Moreover, since an increase in streamwise turbulent fluctuations were deemed to be the responsible entity for reducing vortex swirl [25], the small scale turbulent features released from a fractal endplate may yield a similar effect when drawn into the vortex core. However, due to the re-laminarizing properties of wingtip vortices, it remains to be seen whether these turbulent fluctuations have an effect at large downstream distances. Finally, and directly following on from the previous point, the weakening of the wingtip vortex measured by vortex swirl as well as the larger vortex core radius observed in literature, as a result of chevron shedding edges, has so far only been

examined in close proximity to the wing. The open question therefore remains, if changes to the wingtip vortex extend beyond three chord lengths downstream or whether they remain confined to the early stages of vortex formation? This appears a particularly important question to answer, since both Rossow [26] and Spalart [27], who provide an exhaustive overview of wingtip vortices and their dynamics, argue that changes to the vortex structure are often restricted to short distances behind a wing and do little to alleviate the danger of vortical wakes on downstream aircraft.

The aim of this paper is therefore to experimentally evaluate these four open questions by independently varying the characteristics of the serration pattern applied to the top edge of a winglet. To this end, two triangular patterns of different wavelengths are tested as well as a sinusoidal and multi-scale shedding edge. The winglets are attached to the tip of a NACA-0021 aerofoil which is set at an angle of attack of 3° and 12° to test the impact of the chevron patterns on both a *weaker* and *stronger* vortex, resembling different use cases. To assess the impact of the geometric modifications and to determine which parameter is most important for vortex formation, force balance measurements as well as dye-flow visualization and stereoscopic particle image velocimetry (stereo PIV) are used.

II. Experimental Set-Up

A. Water Tank, Wing and Winglets

The investigation is conducted in the University of Cambridge towing tank facilities shown in figure 2. The water tank is 9 m long and 1 m wide and filled to a height of 0.8 m. The walls and floor are made of glass to provide the optical access to the test section. A servo motor driven carriage moves the length of the tank and its position is measured using an electro-optical sensor with a resolution of 1 mm. The velocity is inferred from numerical differentiation of the position data.

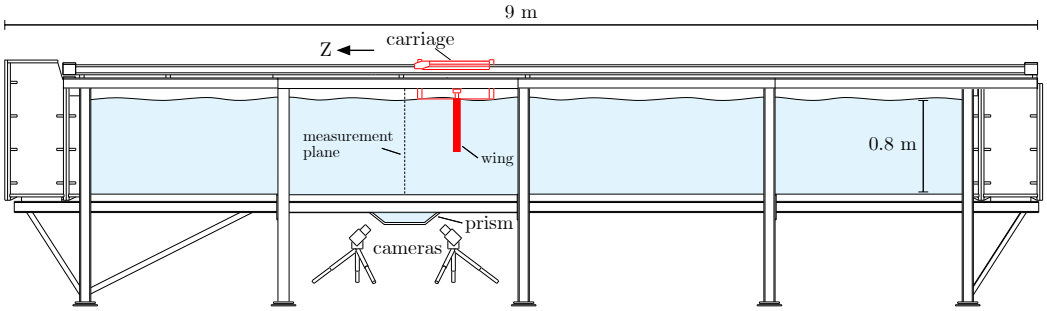

Fig. 2 Overview of the towing tank.

To create the wingtip vortex, a wing is vertically mounted to a force balance, which itself is fixed to the moving carriage. The force balance data uses a Flow Dynamics strain gauge based load cell with a resolution of 0.01 N in both the drag and lift direction. Data is sampled at a rate of 1 kHz using a 16-bit National Instruments data acquisition card.

The wing is rapid-prototyped using ABS-M30 thermoplastic. Three carbon rods extend along the length of the wing to ensure minimal deflection under load. The chord c of the NACA-0021 aerofoil section is 0.1 m, the span of the wing is 0.48 m and a skim plate at the top of the wing extends the effective aspect ratio to 9.6, by imposing a symmetry plane at the water surface. Similar to the wing, the five winglets tested are also 3D-printed using ABS-M30 thermoplastic and all surfaces are sanded down to create a smooth surface finish as well as painted matte black to minimize laser light reflections.

A schematic drawing of the five winglets studied is shown in figure 3. All endplates are 56 mm ($0.56c$) high measured from the chord line, have the same chord length as the wing and are 3 mm thick along their top edge. The leading and trailing edge of the winglets are rounded, whilst the top shedding edges are sharp. The winglets attached to the outer tip of the wing and to ensure representative testing conditions, tape is carefully applied along the split line between the wing and the winglet, to eliminate any leak paths.

The straight-edged (or clean) endplate, referred to as E_{bsl}, acts as the baseline geometry and represents the 'standard' winglet design. The four geometric modifications along the top edge feature a chevron angle φ, measuring the angle between subsequent peaks and troughs, a wavelength λ and a trough to peak distance of $2a$, as schematically indicated in figure 3. All endplates are constructed such that the total surface area, when viewed from the side, is unchanged, whilst varying the length of the shedding edge $\mathcal{P}/c$.

The exact dimensions for all geometries are shown in table 1. In more qualitative terms, endplate E_{tri} has a 'long wavelength' serration pattern applied to its top edge. In contrast, endplate E_{sin} features the same wavelength and amplitude but the sharp serrations are replaced by a sinusoidal profile. Endplate E_{fra} features a fractal iteration i of three [24], where the smallest segment length l_i is 2.21 mm long and aims to introduce a range of lengths scales into the created wingtip vortex. Finally, E_{tri^λ} features the same serrated profile as E_{tri}, where however the wavelength is reduced by half. A schematic illustration of the complete wing-endplate assembly is shown in figure 4 and the geometry of the endplate pattern is summarized in table 1.

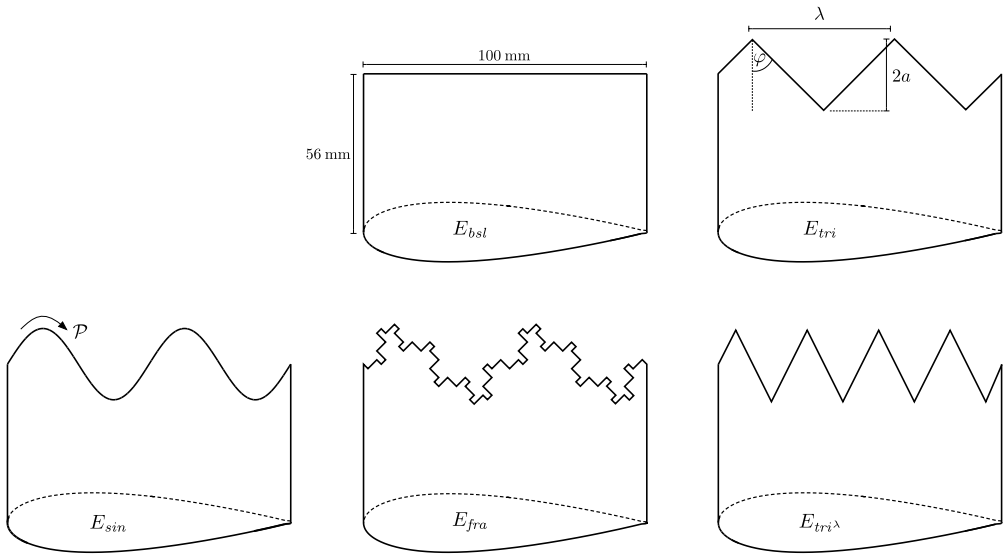

Fig. 3 Winglet geometries

Table 1 Winglet dimensions

D_f: fractal dimension, i: fractal iteration, λ: wavelength of pattern, l_i: segment length
φ: chevron angle, $2a$: amplitude, $\mathcal{P}/c$: ratio between the perimeter and the tip chord.

Endplate	λ (mm)	l_i (mm)	φ (deg)	$2a$ (mm)	$\mathcal{P}/c$
E_{bsl}	-	-	-	-	1
E_{tri}	25	-	45	25.0	1.46
E_{sin}	50	-	45	25.0	1.41
E_{fra}	50	2.21	45	28.13	2.83
E_{tri^λ}	50	-	26	25.0	2.23

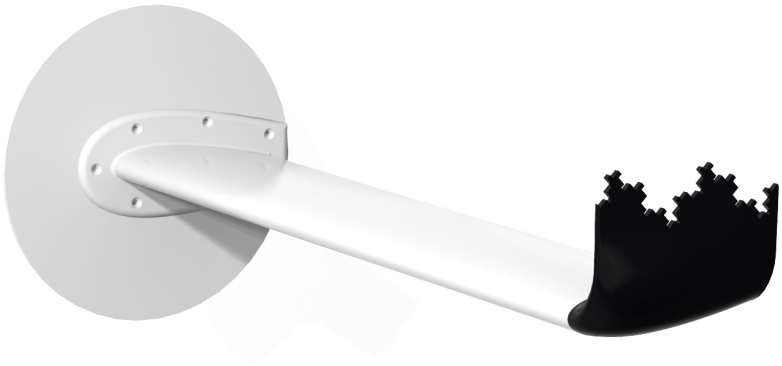

Fig. 4 Rendered illustration of the wing and fractal endplate assembly.

Two cases are explored. For both, the wing rapidly accelerates to a steady-state velocity, U_∞, of 1 ms^{-1} and Reynolds number, Re, of 100 000, which it maintains throughout the complete motion. The angle of attack is set to 3° as well as a more aggressive 12° and each test case is repeated five times. The wing begins its steady-state motion 400 chords upstream of the measurement plane and continues for a further 200 chords thereafter, yielding a total translation distance of 6 m or 600 chord lengths.

When the wing comes to a rest at the end of the tank, the wingtip vortex breaks down. Because it takes a finite amount of time for the associated instability to propagate upstream and 'reach' the measurement plane, dye-flow visualisation and stereo PIV data continue to be sampled during this period. The point at which the instability reaches the measurement plane is at an 'equivalent time' of approximately 70 chord lengths downstream of the wingtip for the baseline winglet and at around 100 chord lengths for the chevron patterned endplates.* Similarly, $\alpha = 3°$ data can be sampled up to 155 chord lengths downstream before the instability is observed at the measurement plane for all winglets.

B. Particle Image Velocimetry

Stereo particle image velocimetry (stereo PIV) is used to assess the dynamics of the wingtip vortex and a schematic illustration of the set-up is shown in figure 5. To measure the flow velocities, the water is seeded with titanium dioxide particles. These are subsequently illuminated by a vertical laser sheet that is normal to the length of the tank and created by a ND:YLF dual cavity Litron PIV300 series laser. Two high speed Phantom M310 cameras are positioned below the tank and observe the laser sheet through a water filled prism and sample a time-series of images at a frequency of 600 Hz. Thereafter, the commercial LaVision Flow Master 2D system is used for the cross correlation process recovering the velocity vectors within the field of view. For this, an adaptive interrogation window with an initial size of 64×64 is employed. In an iterative procedure, it decreases to 24×24 over three passes with an overlap of 50 %. The final velocity vector spacing is 3.2×3.2 mm.

To reduce the optical distortion seen by the cameras, a water filled prism is mounted below the tank, as shown in figure 5. This creates a perpendicular interface between the water and the view of the cameras and thereby enables an optical access with minimal distortions that would otherwise exist due to the mismatch in refractive index between water and air. The open-top prism is firmly pressed against the bottom of the tank and seals with an o-ring, thereby eliminating

*The reason why this instability affects the vortex released from the baseline winglet sooner was not investigated.

any air gap. As a result, the refractive index on either side of the tank floor is equivalent and in turn internal reflections are prevented, which otherwise contaminate the camera images.

To keep the error due to peak locking to a minimum, the particle diameter as seen by the cameras is adjusted to 2 mm [28]. Moreover, to estimate the error of the PIV data, the shift in the correlation peak obtained when mapping the interrogation window back to its original position, according to the calculated velocity vector, is used [29]. This approximates the error to be around 6 % for an individual data set in areas of interest. Since the uncertainty scales with $1\sqrt{n}$, where n is the number of repeated runs, the uncertainty reduces to the order of 3 % as a result of the five repeats for each case.

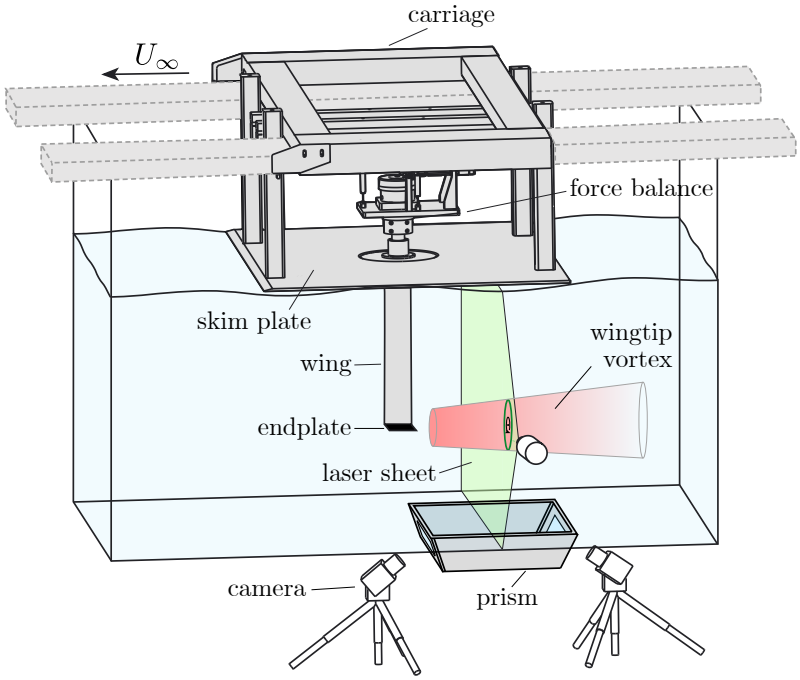

Fig. 5 Overview of the carriage and experimental set-up

C. Dye-Flow Visualisation

To further assess the dynamics of the wingtip vortex, dye-flow visualisation is employed to reveal the intricacies of the vortex development. To visualise the wingtip vortex, the flow is seeded along the top edge of the endplate with a neutrally buoyant dye consisting of soy milk and ethanol. The mixture is fed into the flow via two 1 mm thick tubes that run along the pressure side of the wing and reach the top edge of the winglets. The laser sheet illuminates the dye and the high speed camera captures the evolution of the wingtip vortex.

III. Experimental Wingtip Vortex Results

Force measurements, shown in table 2, reveal that the modifications to the top edge of the winglet have a negligible effect on the the lift and drag experienced by the wing at both $\alpha = 3°$ and $12°$. The following sections therefore assess the vortex structure created by the five endplates tested, where as a result of significant parallels in vortex dynamics at both angles of attack, we mainly focus on the case when the wing is at $\alpha = 12°$ for brevity (as to not subject the reader to an unduly amount of figures).

Table 2 Force results

	$\alpha = 3°$		$\alpha = 12°$	
	C_l	C_d	C_l	C_d
E_{bsl}	0.19	0.051	0.84	0.118
E_{tri}	0.19	0.053	0.84	0.121
E_{sin}	0.19	0.052	0.84	0.119
E_{fra}	0.19	0.053	0.84	0.121
E_{tri^λ}	0.18	0.051	0.83	0.121

A. Dye-Flow Visualisation

To develop an overview of the vortex structure, we first observe the dye-flow visualisation at four different streamwise locations for all endplates at $\alpha = 12°$, as shown in figure 6. The vortex shed by the clean endplate, seen in figures 6a through 6c, shows a tightly wound spiral around a brightly illuminated vortex centre, suggesting that most of the dye was quickly drawn into the core as the vortex formed. This contrasts the dynamics observed at higher translational distances where a significant change in the core structure is visible. An example of this is shown in figure 6d, the vortex core has grown and appears to contain smaller coherent structures, whilst surrounded by unperturbed swirling flow. The instability in the vortex core appears to originate from the end of the tank when wing stops and subsequently propagates upstream to reach the measurement plane. It is therefore worth noting that the results at these high translation distances ($s/c > 70$) are included for completeness but should be viewed with some caution.

The second and third row of figure 6 show the case for the triangular, E_{tri}, and sinusoidal winglet E_{sin}. Already from the outset at $s/c = 10$, the dye is more spread out. This pattern continues downstream, where the dye is smeared out over a greater area and the core is significantly less brightly lit, hinting at an overall more diffuse vortex structure. At $s/c = 100$, the vortex core displays similar properties to those observed for the baseline endplate, where a number of smaller structures are visible.

The vortex shed by the multi-scale winglet E_{fra} is shown in figures 6m through 6p. The fractals seem to have little effect on the vortex structure in comparison to E_{tri} shown in the second row of figure 6. In contrast to this, changing the wavelength of the chevron pattern appears to have the most significant effect on the wingtip vortex structure. The vortex released by E_{tri^λ} seen in figures 6q through 6t, appears the most spread out at every downstream location, as inferred from the homogeneous distribution of the dye within the vortex. This is especially obvious when comparing the brightness of the core. Whereas all other vortices released from the other endplates show a distinct change in brightness between the centre of the vortex and the surrounding swirling flow, no such variation is observable for E_{tri^λ}.

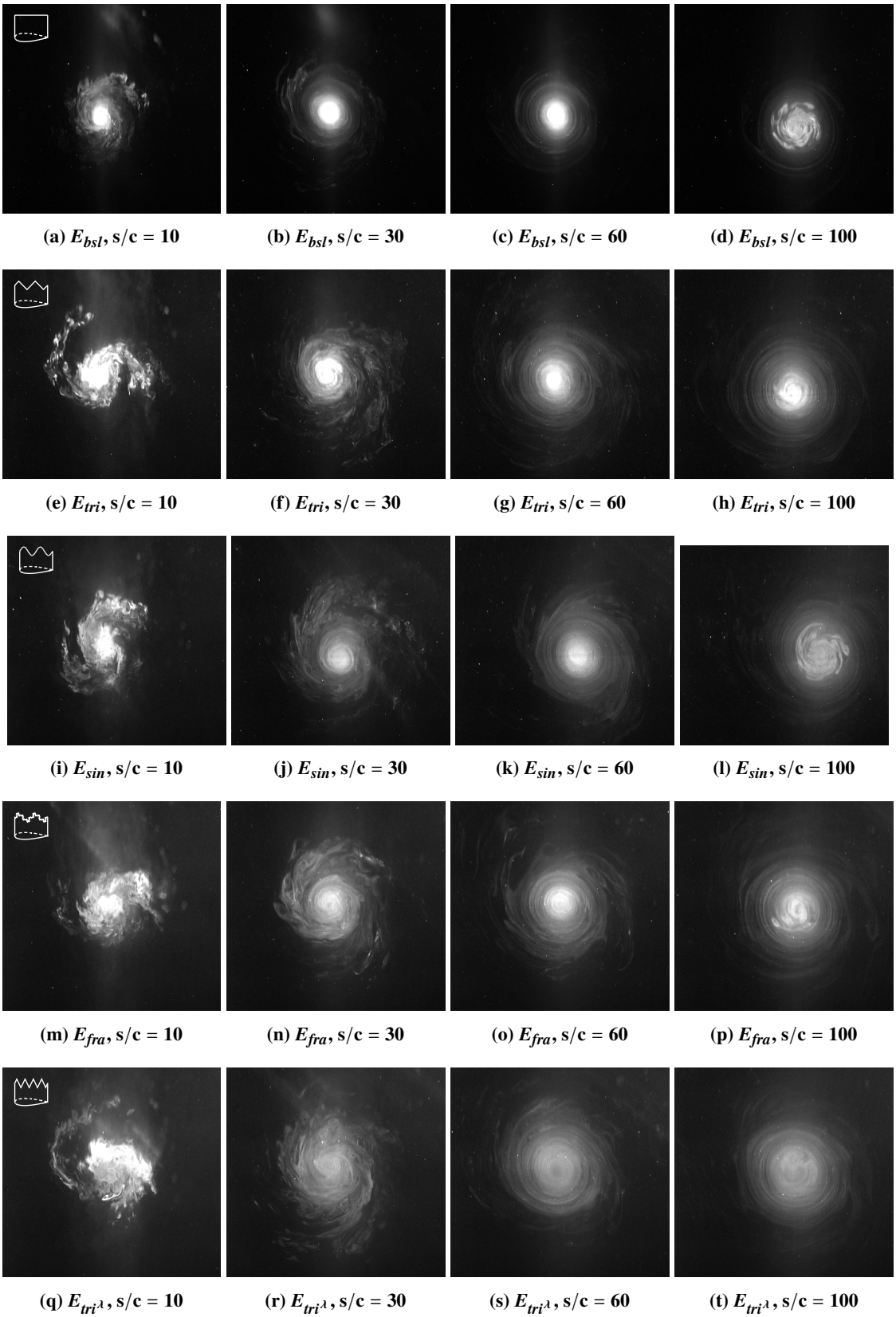

(a) E_{bsl}, s/c = 10 (b) E_{bsl}, s/c = 30 (c) E_{bsl}, s/c = 60 (d) E_{bsl}, s/c = 100

(e) E_{tri}, s/c = 10 (f) E_{tri}, s/c = 30 (g) E_{tri}, s/c = 60 (h) E_{tri}, s/c = 100

(i) E_{sin}, s/c = 10 (j) E_{sin}, s/c = 30 (k) E_{sin}, s/c = 60 (l) E_{sin}, s/c = 100

(m) E_{fra}, s/c = 10 (n) E_{fra}, s/c = 30 (o) E_{fra}, s/c = 60 (p) E_{fra}, s/c = 100

(q) $E_{tri^{\lambda}}$, s/c = 10 (r) $E_{tri^{\lambda}}$, s/c = 30 (s) $E_{tri^{\lambda}}$, s/c = 60 (t) $E_{tri^{\lambda}}$, s/c = 100

Fig. 6 Dye-flow visualisation of the wingtip vortex, $\alpha = 12°$.

B. Vorticity Iso-Surfaces

A more in depth assessment of the vortex structure, resulting from the individual winglets, can be made by plotting iso-contours of vorticity, colour coded by velocity in the y-direction. The results of this are shown for all endplates in figure 7, for a region spanning from the wing until 40 chord length downstream. As expected, a single vortex forms along the top edge of the baseline winglet and is released into the flow. In contrast to this, all other endplates show the creation of two identifiable vortices that shed from the peaks and troughs of the endplates and merge into a single vortex within 10 chord lengths of the trailing edge, where the short-wavelength pattern appears to create the most distinctive vortex pair. The mutual interaction of the vortices and subsequent coalescence is interesting since such processes have shown to lead to a larger vortex core and a more diffuse vortex structure [30]. This may therefore in turn begin to explain the observations from figure 6, where especially E_{tri^λ} was found to feature a much less coherent vortex structure compared to E_{bsl}, where only a single vortex is created.

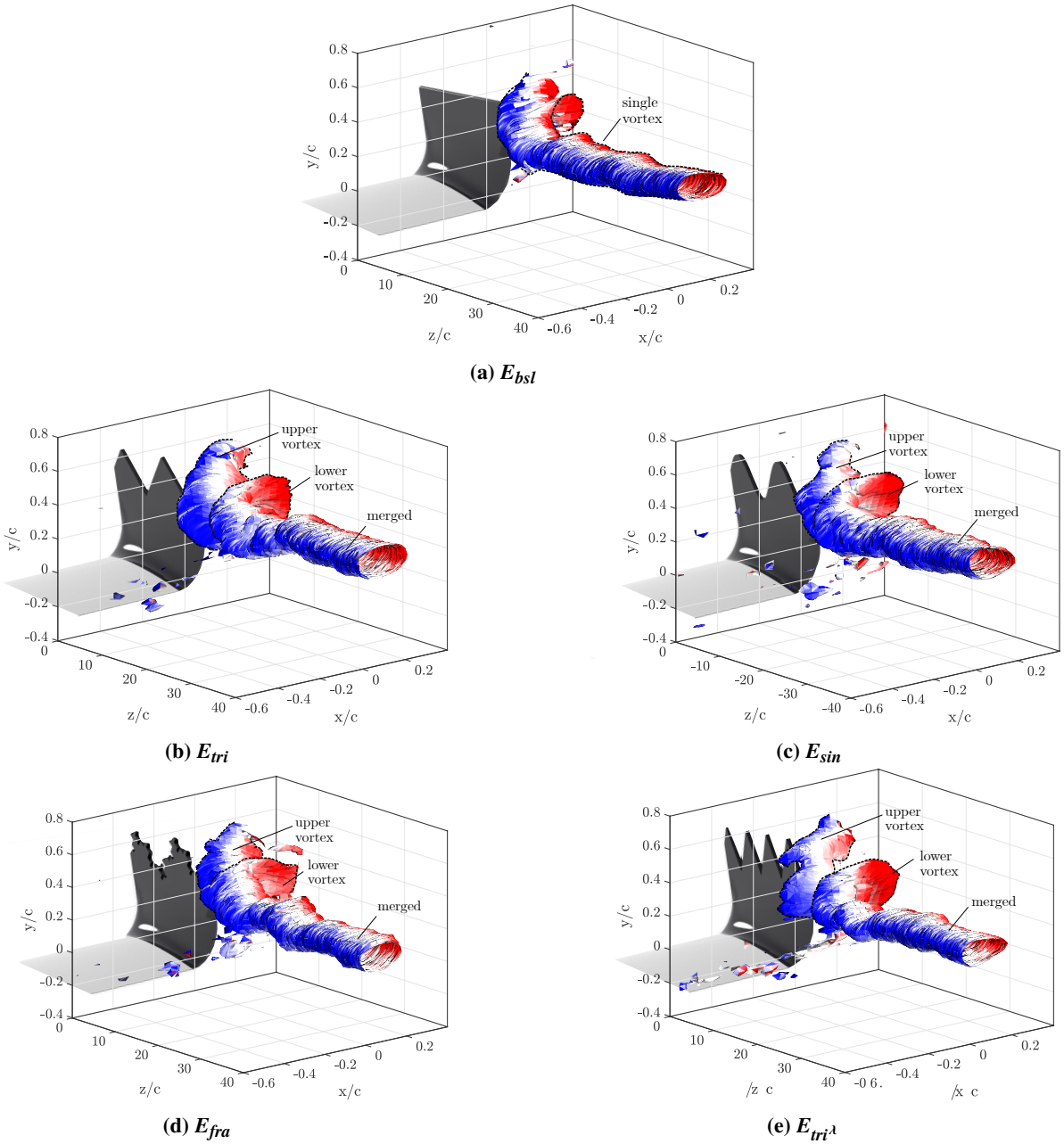

(a) E_{bsl}

(b) E_{tri}

(c) E_{sin}

(d) E_{fra}

(e) E_{tri^λ}

Fig. 7 Vorticity contours coloured by vertical velocity at $\pm 0.15/U_\infty$.

C. Circulation

The circulation when the wing is at both an angle of attack of 3° and 12° for each released vortex is shown in figure 8. Here, little variation of circulation is observed both at any given downstream distance as well as between vortices created by individual winglets. The observed consistency matches the force results, in that each wing experiences an equal amount of lift and thus features a similar bound circulation.

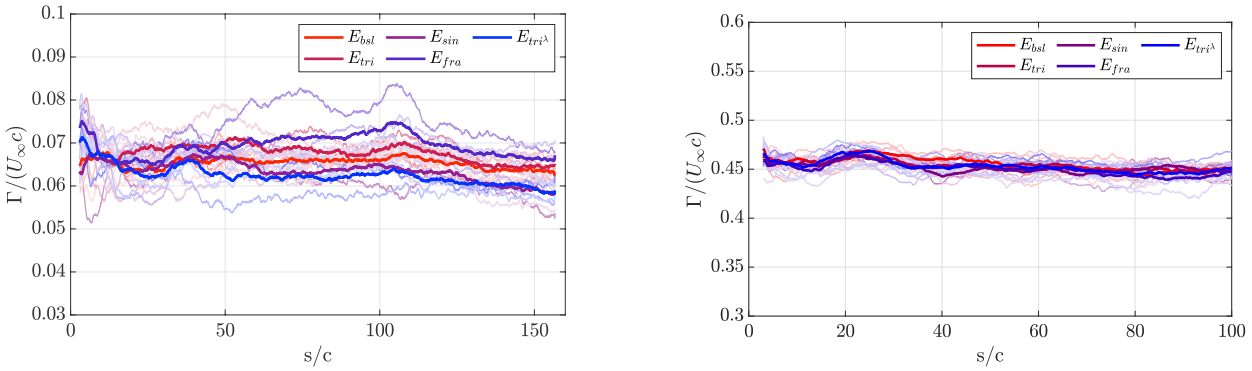

(a) α = 3° **(b) α = 12°**

Fig. 8 Circulation of the vortex released by the individual endplates.

D. Vorticity Contours

To further interrogate the vortex structures, we can plot individual slices of the vorticity distribution at different stream normal planes, as shown in figure 9. In accordance with the results seen so far, a single coherent vortex is shed by the 'clean' baseline endplate and slowly loses strength as it moves away from the wing, as seen in figure 9a. In contrast to this, vorticity contours for the modified winglets all show the creation of two initial vortices (most clearly visible for E_{tri^λ}) that are released from the peaks an troughs of the serration pattern. These merge with downstream distance and lead to vorticity contours of reduced intensity compared to the baseline winglet E_{bsl}. This corroborates the flow visualisation results from figure 6, and suggests that the modified shedding edge has a noticeable effect on the vortex structure, not only just behind the wing but that this persists for larger downstream distances.

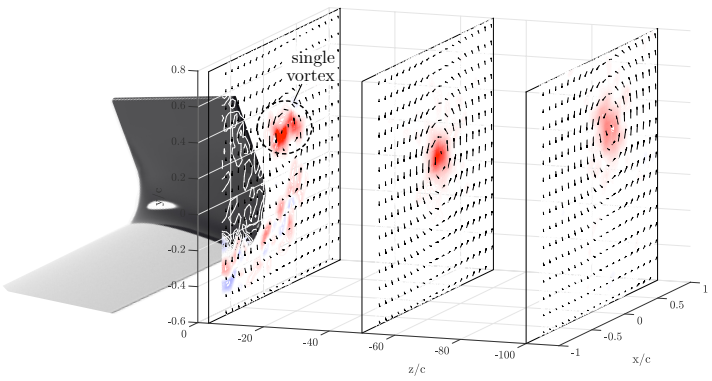

(a) E_{bsl}

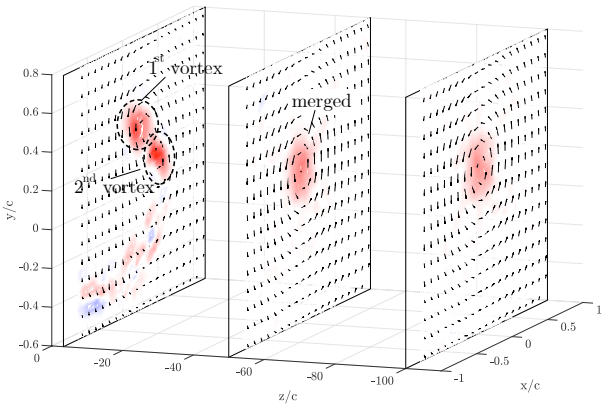

(b) E_{tri}

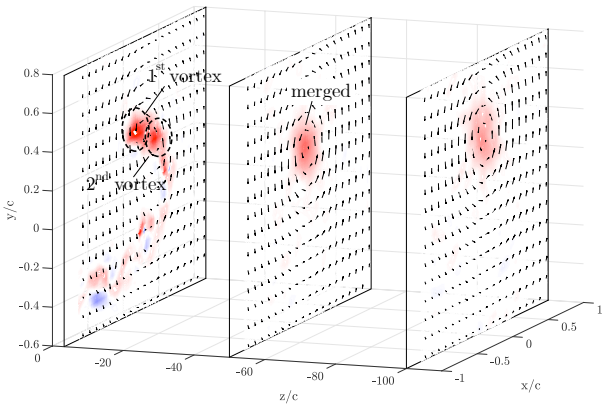

(c) E_{sin}

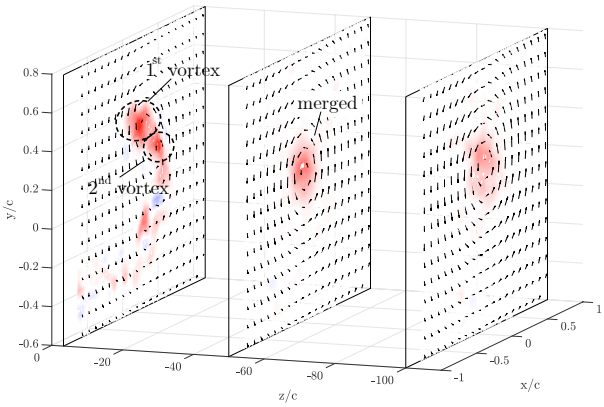

(d) E_{fra}

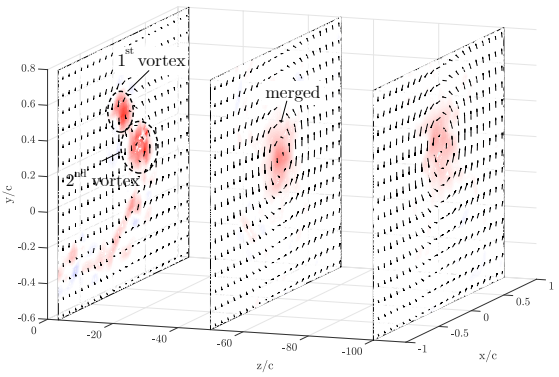

(e) $E_{tri^{\lambda}}$

Fig. 9 Normalised vorticity contours at selected streamwise positions, s/c = 3, 50 and 100, when α = 12°.

E. Swirl Velocity

To assess the wingtip vortices from a more quantitative perspective, the maximum swirl velocity $\overline{u}_{\theta_{max}}$ for each distance downstream of the wingtip can be extracted from PIV data,

$$\overline{u}_{\theta_{max}} = \frac{1}{N}\sum_{j=1}^{N} u^{j}_{\theta_{max}}. \tag{1}$$

To do so, we take the average of the maximum tangential velocity $u_{\theta_{max}}$ measured at N positions along the circumference of the vortex, where the centre of the vortex is found by fitting a Lamb-Oseen vortex [31] to the velocity field. A schematic representation of this process is shown in figure 10a. Moreover, because of the discrete nature of the PIV measurements, $u_{\theta_{max}}$ at each angular position is obtained from a linear interpolation of the velocity field. Using $\overline{u}_{\theta_{max}}$, we can further estimate the core radius r_c of the vortex by assessing the radial distance at which $\overline{u}_{\theta_{max}}$ occurs.

Further to this, the radial velocity distribution can be assessed by evaluating the average circumferential $\overline{u}_{\theta_{avg}}$ and axial velocity $\overline{u}_{z_{avg}}$ along a circle of variable radius, as illustrated in figure 10b. Similar to the calculation of $\overline{u}_{\theta_{max}}$, 100 circumferential points are used to determine $\overline{u}_{\theta_{avg}}$ and $\overline{u}_{z_{avg}}$, where the radial distance from the vortex centre extends to $r/c = 0.6$ in steps of $0.02c$.

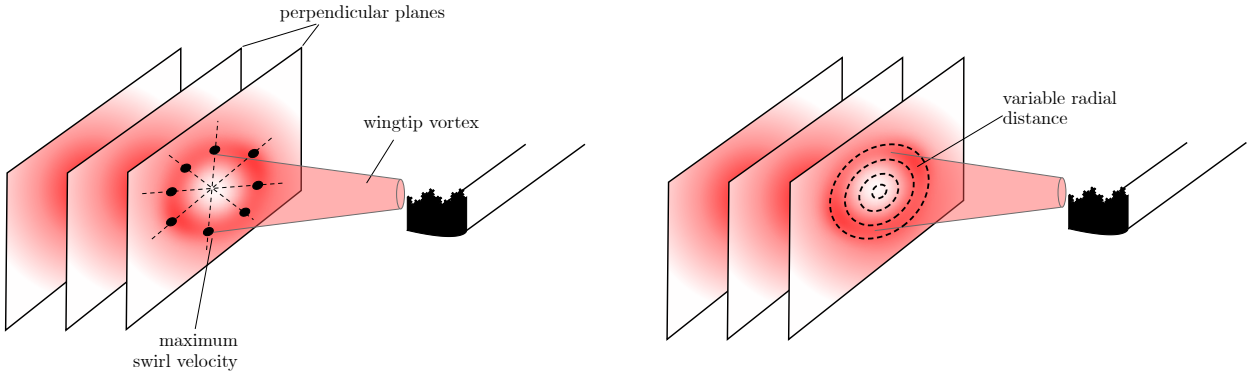

(a) Maximum swirl velocity $\overline{u}_{\theta_{max}}$

(b) Average tangential, $\overline{u}_{\theta_{avg}}$, and axial velocity, $\overline{u}_{z_{avg}}$

Fig. 10 Schematic illustration of the calculation of vortex quantities with downstream distance.

Figure 11 shows the maximum swirl velocity $\overline{u}_{\theta_{max}}$ as well as the vortex core radius r_c for the vortices released by all winglets. At a wing angle of attack of 12°, $\overline{u}_{\theta_{max}}$ is reduced for all modified endplates compared to the vortex shed by the baseline winglet. The most significant reduction comes from E_{tri^λ}, which reduces the swirl velocity by around 20 % and is thus consistent with the previous observations, that shortening the wavelength of the serrations is the dominant entity modifying the vortex structure. The triangular, sinusoidal and multi-scale modifications to the shedding edge instead show a reduced impact on $\overline{u}_{\theta_{max}}$ compared to E_{tri^λ}, with no noticeable difference between the three geometries.

It is further interesting to note that the swirl velocity for the vortex released from the baseline winglet shows a continuous decrease up until around 70 chords downstream, after which a sudden step change occurs and a faster dissipation ensues. This change is consistent with the vortex core undergoing a visible transformation in the dye-flow visualisation, which we recall appeared to have been triggered by the finite length of the tank. The data beyond $s/c \approx 70$ for E_{bsl} is therefore only included for completeness and should be treated with caution. Nevertheless, at $s/c = 70$ the chevron endplates still appear to create a weaker vortex when based on maximum swirl velocity.

A further point to note is that whilst the baseline endplate exhibits a steady rate of decay of $\overline{u}_{\theta_{max}}$, the maximum swirl velocity for the chevron endplates remains almost unchanged downstream of 10 chord lengths. This suggests that a significant reduction in swirl velocity may be attributed to the merging of the two vortex structures released from the peaks and troughs of the winglets, which occurs upstream of $s/c = 10$. Once this merging process is complete, little further decay appears to take place.

Further to assessing the maximum swirl velocity, we can extract the radial distance at which $\overline{u}_{\theta_{max}}$ occurs (a measure of the vortex core) and the results are plotted in figure 11b. Here we observe that the size of the vortex core appears to be inversely proportional to the maximum swirl velocity. Whilst the baseline winglet showed the highest $\overline{u}_{\theta_{max}}$, this occurs at the smallest radial distance. The vortices shed by the triangular, sinusoidal and fractal endplates feature a larger core whilst remaining similar to each other, with the reduction in wavelength for E_{tri^λ} yielding the largest core. Moreover, once more, whilst the core radius grows only slowly for the modified winglets, the vortex released from the baseline endplate exhibits a more rapid increase as well as step change at around $s/c = 70$. This coincides with the previously

noted sudden change in $\overline{u}_{\theta_{max}}$ and the transformation of the core observed in dye-flow visualisation.

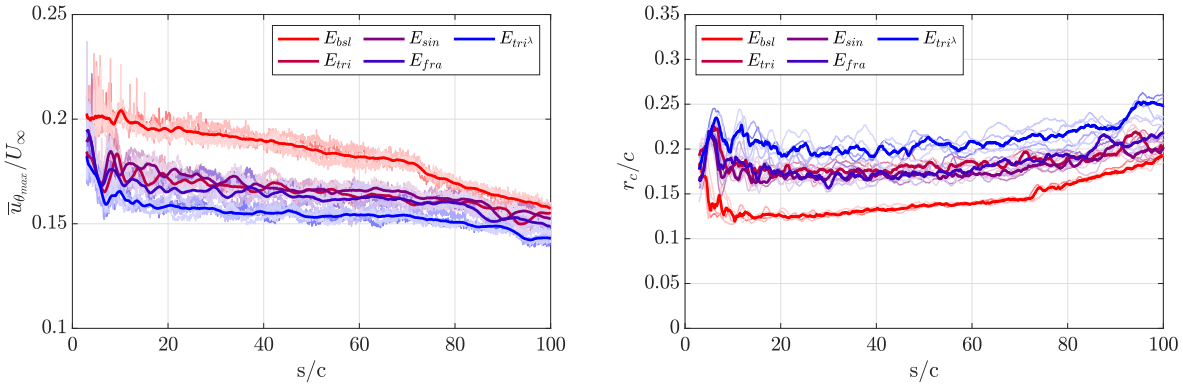

(a) Maximum swirl velocity, $\overline{u}_{\theta_{max}}$ **(b) Core radius, r_c**

Fig. 11 Maximum swirl velocity and the core radius at $\alpha = 12°$ with downstream distance.

We now evaluate the maximum swirl velocity and the vortex core radius when $\alpha = 3°$. This helps evaluate whether the reduction in $\overline{u}_{\theta_{max}}$ is isolated to the more powerful vortex created at $\alpha = 12°$ or whether this is a more general phenomenon. With regards to this, figure 12a shows the variation of $\overline{u}_{\theta_{max}}$ up to 155 chord lengths downstream for all winglets. Here we observe, that similar to the higher angle of attack, the baseline winglet once more creates a vortex that has the highest maximum swirl velocity, whilst the the vortex shed from E_{tri^λ} creates the weakest vortex, featuring an approximate 45% reduction in maximum swirl velocity between 20 and 155 chord lengths downstream of the wing. Similar to what was observed previously, the triangular and sinusoidal winglet create an almost equal reduction in swirl velocity, whereas the introduction of the fractal iteration actually reduces the impact of the chevron pattern. Moreover, beyond the first 10 chord lengths, all vortices experience a comparable rate of decay of maximum swirl velocity. The vortex core follows the same trend as observed for the wing at 12° albeit with slightly more noise, where the maximum and minimum core sizes are featured by the vortices released by E_{tri^λ} and E_{bsl} respectively.

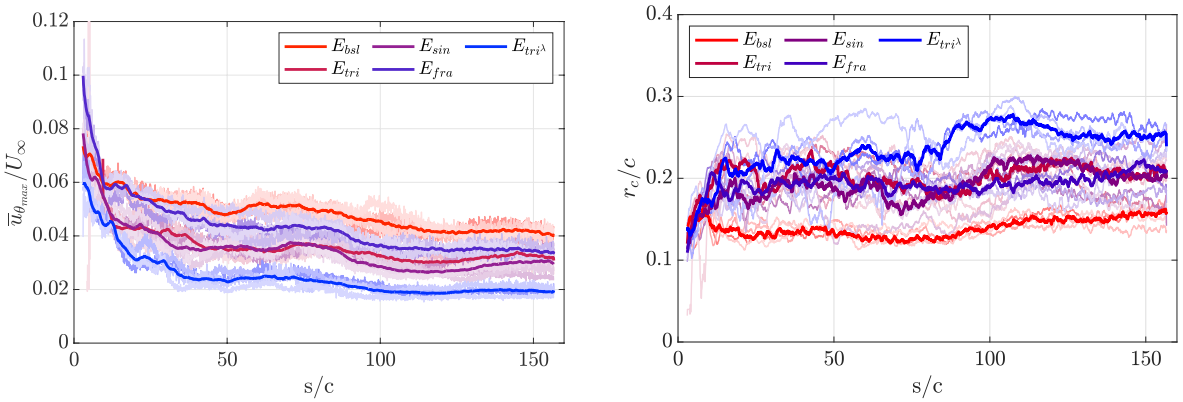

(a) Maximum swirl velocity $\overline{u}_{\theta_{max}}$ **(b) Core radius, r_c**

Fig. 12 Maximum swirl velocity and the core radius at $\alpha = 3°$ with downstream distance.

To further assess the radial velocity, we use the methodology outlined previously to determine the average swirl velocity $\overline{u}_{\theta_{avg}}$ at each radial position centred on the vortex core. The results for all vortices shed by the individual winglets are shown in figure 13 for four stream-normal planes located at $s/c = 3, 10, 30$ and 70. Just downstream of the wing at $s/c = 3$ we observe a *double peak* or plateau region at low radial distances before the characteristic decline in $\overline{u}_{\theta_{avg}}$ is measured for all chevron winglets. This suggests that at this point the shed vortex is not yet fully formed and matches the results seen from the iso- and planar vorticity contours seen earlier. In contrast, the vortex shed from the baseline

endplate exhibits a single velocity peak, indicating a mature vortex. Furthermore, at this streamline position as well as at any further position downstream, the peak swirl velocity and the general average tangential velocity is always maximum for the vortex shed by the baseline endplate. The smallest values, as has become characteristic by now, are consistently seen for the vortex released from $E_{tri^{\lambda}}$.

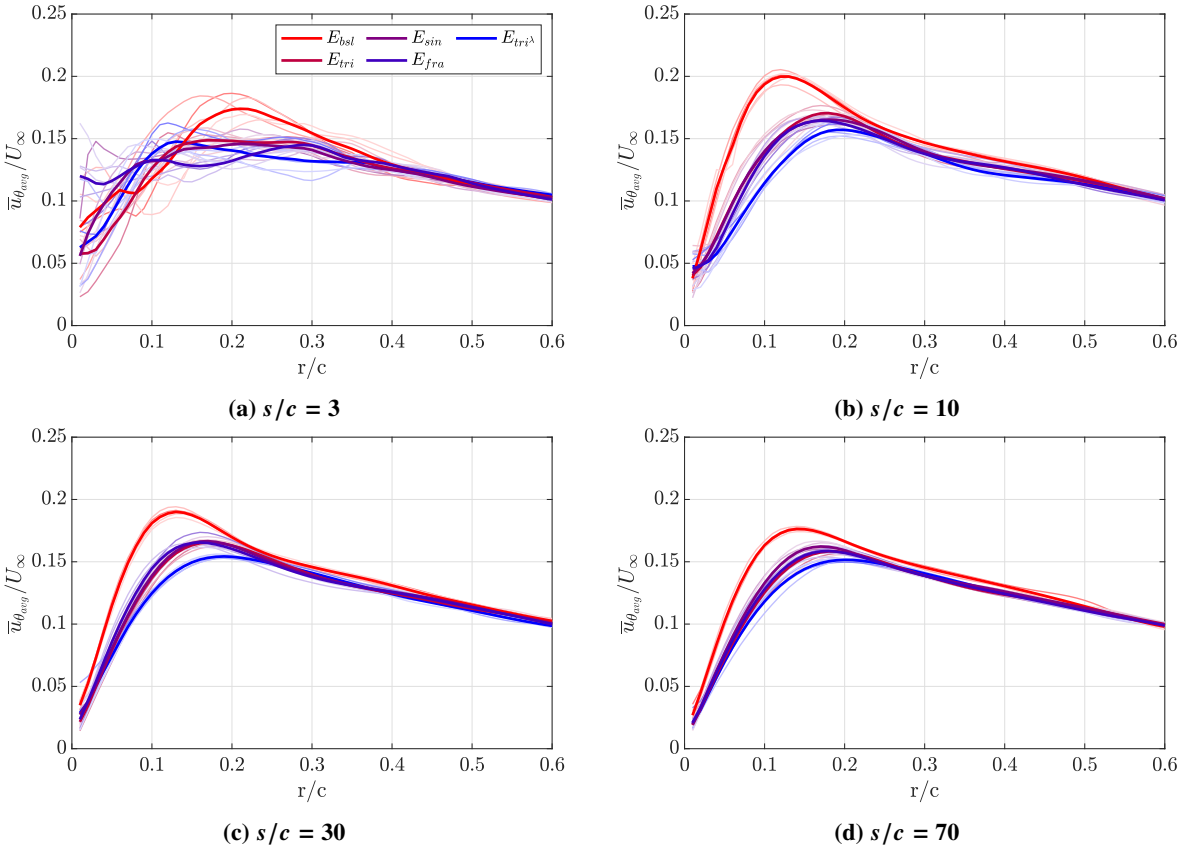

(a) $s/c = 3$ **(b)** $s/c = 10$

(c) $s/c = 30$ **(d)** $s/c = 70$

Fig. 13 $\overline{u}_{\theta_{avg}}$ **distribution at** $\alpha = 12°$.

To assess the impact off the trade of between swirl velocity and an increased vortex core, we can integrate the non-dimensional velocity profile with non-dimensional radial position to arrive at a more objective measure of vortex strength based on swirl velocity [25],

$$\psi = \int_0^3 \frac{\overline{u}_{\theta_{avg}}}{U_{\infty}} d\left(r/r_c\right). \tag{2}$$

The development of ψ is shown in figure 14. The overall trends match those of the maximum swirl velocity shown in figures 11 and 12, namely that:

- The vortex released from the baseline winglet features the highest swirl strength parameter, whilst the vortex released from the short-wavelength serration pattern $E_{tri^{\lambda}}$ reduces ψ by about 65 % and is the lowest out of all cases.
- A rapid decay in ψ is observed until around 10 chord lengths downstream of the wing, after which the rate of decay is similar for all vortices.
- Smoothing the shedding edge or applying a fractal pattern appears to have little influence on the overall vortex structure.

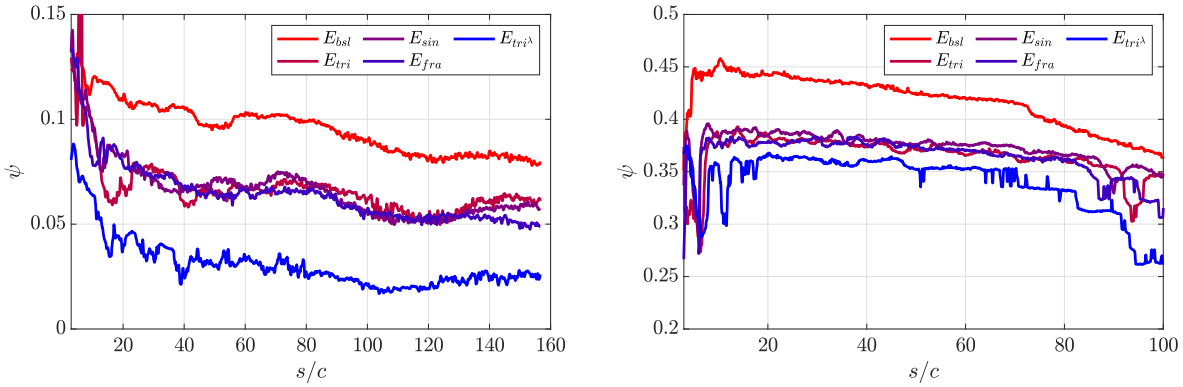

(a) α = 3° **(b) α = 12°**

Fig. 14 Vortex strength parameter ψ with downstream distance.

F. Axial Velocity

The final metric the reader is subjected to is the axial velocity of the wingtip vortex when the wing is at 12° and this is only to highlight the fact that whilst at high angles of attack, the baseline winglet creates a velocity excess directly behind the wing (s/c = 3), as seen in figure 15a. The chevron patterns reduce this to a more neutral flow or a velocity deficit, as also visible in figures 15a. By 5.5 chord lengths downstream of the wing, the axial velocity for all serrated winglets shows a velocity deficit, whilst it remains neutral for E_{bls}. The precise reasons behind the velocity excess and deficit cannot be established from the current data but similar observations in the literature have been explained in terms of the turbulence levels inside the viscous core [30].

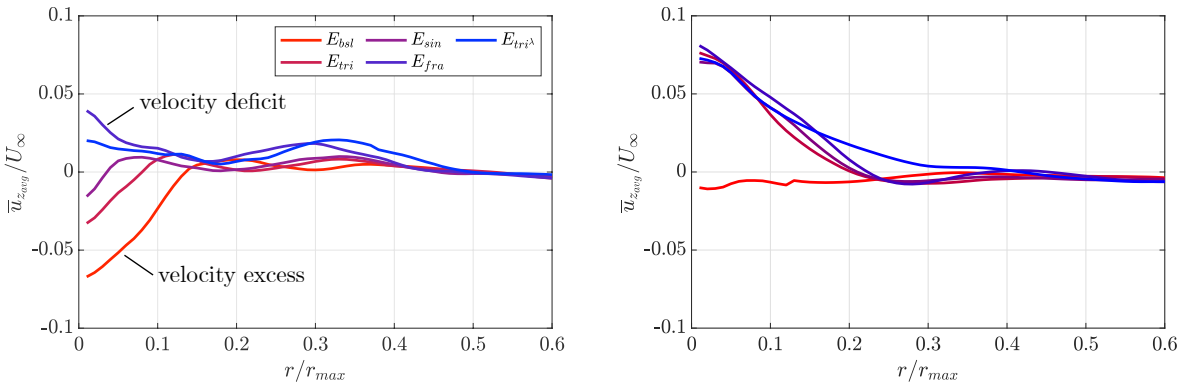

(a) s/c = 3 **(b) s/c = 5.5**

Fig. 15 $\overline{u}_{z_{avg}}$ distribution at α = 12°.

G. General Inferences

From assessing the general impact of the chevron pattern in comparison to the clean shedding edge, it is found that all serrated winglets shed two distinct vortices that merge roughly 10 chord lengths behind the wing. Observing the downstream development of the vortex properties, we clearly see that the winglet serrations have a measurable effect on the vortex up to at least 155 (α = 3°) and 70 (α = 12°) chord lengths downstream of the wingtip, compared to a clean shedding edge. Thus, changes to the vortex structure are not confined to the near field. Whilst the initial rapid decay of swirl velocity can be strongly affected by the wingtip geometry, the subsequent more gentle reduction exhibits very similar behaviour for each case studied. This strongly suggests that the merging of the two vortices shed from the peaks and troughs of the serrated winglets is the driving factor behind the change in vortex properties. The merging

of these vortices is likely to feature an entrainment of the surrounding wake into the newly-created vortex core [33], which would cause vorticity to spread and create a more diffuse vortex. Following this merging, the similarity in vortex development between different cases and the fact that the decay is so gradual, suggests that no heightened turbulent activity or mixing is taking place. This behaviour appears to be consistent with the re-laminarization processes proposed by Bradshaw [16], Jacquin and Pantano [17], Devenport et al. [33], but additional measurements of the turbulent fluctuations themselves would be required to confirm this hypothesis.

Further to this, the study aimed to answer three other questions about the effect of the geometric modifications to the shedding edges. The first was to assess what impact a sharp or smoothly varying profile has on the wingtip vortex. We conclude that the exact shape of single-scale serrations are of secondary importance and do not have an overarching effect on vortex structure based on the qualitative dye-flow visualisation and quantitative velocity measurements of the vortices released by the triangular E_{tri} and sinusoidal winglet E_{sin}, which showed little difference between the two. The second point to assess was the effect of a multi-scale pattern along the shedding edge. The effect of this also appears of secondary nature, since the swirl strength parameter and vortex radius of E_{tri} and E_{fra} show an almost identical development.

In contrast to these first two geometric changes, altering the wavelength of the serration pattern (and thus the chevron angle) has a significant effect on the final vortex. Furthermore, the maximum swirl and swirl strength parameter of the vortex released by $E_{tri\lambda}$ are significantly reduced compared to those of E_{tri}. The vortex appears qualitatively more homogeneous, as revealed by the dye-flow visualisation in figure 6, and the vorticity contours highlight that the shorter wavelength pattern creates a distinctive co-rotating vortex structure in close proximity to the wingtip.

IV. Conclusion

This paper evaluates the effect that chevron patterns, applied to the top edge of a winglet, have on the wingtip vortex using dye-flow visualisation as well as stereo particle image velocimetry. The wing is at an angle of attack of 3° and 12° and towed at a speed of 1 ms^{-1}, giving a chord-based Reynolds number of 100 000. Force measurements show a negligible influence of the chevron patterns.

Assessing the vortex structure, the chevron patterns are found to release two distinct vortices, forming from the peaks and troughs of the serrations, which merge roughly 10 chord lengths downstream of the wing. In turn, all modifications of the shedding edge studied lead to a lower vortex strength when based on maximum swirl velocity or swirl strength (the swirl velocity integrated along the radial direction of the vortex), which persists until at least 155 and 70 chord lengths downstream, compared to a vortex shed from a straight edge, when the wing is at 3° and 12°, respectively. Moreover, after an initial rapid reduction of the vortex swirl velocity, when released from the chevron winglets, little further variation in vortex development is observed with downstream distance past 10 chord lengths behind the wingtip and between different cases. The merging process of the two co-rotating vortices shed by the serrated winglets is thus thought to be the dominant process by which the properties of the wingtip vortex are modified.

The shape of the serrations, whether sharp or sinusoidal, seems to have little effect on the shed vortex. Similarly, superposing a multi-scale pattern onto triangular serrations also appears to have a negligible effect on the released vortex. Instead, changing the wavelength of the serrations (and thus the chevron angle) has a distinct influence and significantly reduces the maximum swirl velocity as well as the swirl strength, whilst increasing core radius, suggesting that this is the most promising approach to modifying the vortex structure.

Acknowledgments

The authors would like to acknowledge the Engineering and Physical Science Research Council (EPSRC).

References

[1] Simpson, C. E., Babinsky, H., Harvey, J. K., and Corkery, S., "Detecting vortices within unsteady flows when using single-shot PIV," *Experiments in Fluids*, Vol. 59, No. 8, 2018, pp. 1–13.

[2] Read, S., and Hynes, T., "Effect of a winglet on open rotor aerodynamics and tip vortex interaction," *49th AIAA/ASME/SAE/ASEE Joint Propulsion Conference*, Vol. 1 PartF, 2013, pp. 1–24.

[3] Saravanakumar, J., Shameem, C. A., and Venkatesh, T. N., "Development of a potential vortex-hazard index to predict cruise-level wake turbulence encounters," *Sadhana - Academy Proceedings in Engineering Sciences*, Vol. 44, No. 4, 2019, pp. 1–11.

[4] Sarpkaya, T., and Daly, J. J., "Effect of ambient turbulence on trailing vortices," *Journal of Aircraft*, Vol. 24, No. 6, 1987, pp. 399–404.

[5] Melander, M. V., and Hussain, F., "Coupling between a coherent structure and fine-scale turbulence," *Physical Review E*, Vol. 48, No. 4, 1993, pp. 2669–2689.

[6] Holzäpfel, F., Hofbauer, T., Darracq, D., Moet, H., Garnier, F., and Gago, C. F., "Analysis of wake vortex decay mechanisms in the atmosphere," *Aerospace Science and Technology*, Vol. 7, No. 4, 2003, pp. 263–275.

[7] Bailey, S. C., and Tavoularis, S., "Measurements of the velocity field of a wing-tip vortex, wandering in grid turbulence," *Journal of Fluid Mechanics*, Vol. 601, 2008, pp. 281–315.

[8] Jupp, J., "Wing aerodynamics and the science of compromise," *Aeronautical Journal*, Vol. 105, No. 1053, 2001, pp. 633–641.

[9] Chambers, J. R., *Concept to reality: Contributions of the Langley Research Center to U.S. Civil Aircraft of the 1990s*, SUPPL., NASA History Series, 2003.

[10] Spillman, J. J., "Wing Tip Sails; Progress To Date and Future Developments." *Aeronautical Journal*, Vol. 91, No. 910, 1987, pp. 445–453.

[11] Kravchenko, S. A., "Wing Tip Lifting Surfaces: Aerodynamic Design and Comparative Analysis," *Aircraft Engineering, Technology, and Operations Congress*, 1995.

[12] Guerrero, J. E., Maestro, D., and Bottaro, A., "Biomimetic spiroid winglets for lift and drag control," *Comptes Rendus - Mecanique*, Vol. 340, No. 1-2, 2012, pp. 67–80.

[13] Céron-Muñoz, H. D., Cosin, R., Coimbra, R. F., Correa, L. G., and Catalano, F. M., "Experimental investigation of wing-tip devices on the reduction of induced drag," *Journal of Aircraft*, Vol. 50, No. 2, 2013, pp. 441–449.

[14] Heyes, A. L., and Smith, D. A., "Modification of a wing tip vortex by vortex generators," *Aerospace Science and Technology*, Vol. 9, No. 6, 2005, pp. 469–475.

[15] Smith, H. C., "Method for reducing the tangential velocities in aircraft trailing vortices," *Journal of Aircraft*, Vol. 17, No. 12, 1980, pp. 861–866.

[16] Bradshaw, P., "The analogy between streamline curvature and buoyancy in turbulent shear flow," *Journal of Fluid Mechanics*, Vol. 36, No. 1, 1969, pp. 177–191.

[17] Jacquin, L., and Pantano, C., "On the persistence of trailing vortices," *Journal of Fluid Mechanics*, Vol. 471, 2002, pp. 159–168.

[18] Nedić, J., Ganapathisubramani, B., and Vassilicos, J. C., "Drag and near wake characteristics of flat plates normal to the flow with fractal edge geometries," *Fluid Dynamics Research*, Vol. 45, No. 6, 2013.

[19] Nedić, J., Supponen, O., Ganapathisubramani, B., and Vassilicos, J. C., "Geometrical influence on vortex shedding in turbulent axisymmetric wakes," *Physics of Fluids*, Vol. 27, No. 3, 2015.

[20] Cafiero, G., Castrillo, G., Greco, C. S., and Astarita, T., "On the effects of square-fractal turbulators on the flow field generated by a synthetic jet actuator," *Experimental Thermal and Fluid Science*, Vol. 102, No. September 2018, 2019, pp. 302–315.

[21] Phan, H. T., Caney, N., Marty, P., Colasson, S., and Gavillet, J., "Surface wettability control by nanocoating: The effects on pool boiling heat transfer and nucleation mechanism," *International Journal of Heat and Mass Transfer*, Vol. 52, No. 23-24, 2009, pp. 5459–5471.

[22] Nedi, J., and Vassilicos, J. C., "Vortex shedding and aerodynamic performance of airfoil with multiscale trailing-edge modifications," *AIAA Journal*, Vol. 52, No. 11, 2015, pp. 3240–3250.

[23] Prigent, S. L., Buxton, O. R., and Bruce, P. J., "Coherent structures shed by multiscale cut-in trailing edge serrations on lifting wings," *Physics of Fluids*, Vol. 29, No. 7, 2017.

[24] Gehlert, P., Cherfane, Z., Cafiero, G., and Vassilicos, J. C., "Effect of Multiscale Endplates on Wing-Tip Vortex," *AIAA Journal*, Vol. 59, No. 5, 2021, pp. 1614–1628.

[25] Goyal, A., and Nedić, J., "Near field of a vortex generated by chevron-tipped flat plates," *AIAA Journal*, Vol. 59, No. 2, 2021, pp. 546–558.

[26] Rossow, V. J., "Lift-generated vortex wakes of subsonic transport aircraft," *Progress in Aerospace Sciences*, Vol. 35, No. 6, 1999, pp. 507–660.

[27] Spalart, P. R., "Airplane Trailing Vortices," *Annual Review of Fluid Mechanics*, Vol. 30, No. 1, 1998, pp. 107–138.

[28] Westerweel, J., "Fundamentals of Digital Particle Image Velocimetry," *Meas. Sci. Technol*, Vol. 8, 1997, pp. 1379–1392.

[29] Wieneke, B., "PIV Uncertainty Quantification from Correlation Statistics," *Measurement Science and Technology*, Vol. 26, No. 7, 2015, p. 074002.

[30] Spalart, P. R., "Airplane trailing vortices," *Annual Review of Fluid Mechanics*, Vol. 30, 1998, pp. 107–138.

[31] Lamb, H., *Hydrodynamics*, 1932.

[32] Cerretelli, C., and Williamson, C. H., "The physical mechanism for vortex merging," *Journal of Fluid Mechanics*, Vol. 475, 2003, pp. 41–77.

[33] Devenport, W. J., Vogel, C. M., and Zsoldos, J. S., "Flow structure produced by the interaction and merger of a pair of co-rotating wing-tip vortices," *Journal of Fluid Mechanics*, Vol. 394, 1999, pp. 357–377.

[34] Gehlert, P., Cherfane, Z., Cafiero, G., and Vassilicos, J. C., "Effect of multiscale endplates on wing-tip vortex," *AIAA Journal*, Vol. 59, No. 5, 2021.